ULTRASONIC IMAGING **20**, 81- 102 (1998)

Multi-Angle Compound Imaging

SØREN K. JESPERSEN[1,2], JENS E. WILHJELM[1] AND HENRIK SILLESEN[3]

[1]*CADUS, Department of Information Technology*
Technical University of Denmark, Bldg. 344
DK-2800 Lyngby, Denmark

[2]*B-K Medical, Sandtoften 9*
DK-2820 Gentofte, Denmark

[3]*CADUS, Department of Vascular Surgery*
Gentofte Hospital
University of Copenhagen
DK-2900 Hellerup, Denmark
skj@it.dtu.dk

This paper reports on a scanning technique, denoted multi-angle compound imaging (MACI), using spatial compounding. The MACI method also contains elements of frequency compounding, as the transmit frequency is lowered for the highest beam angles in order to reduce grating lobes. Compared to conventional B-mode imaging MACI offers better defined tissue boundaries and lower variance of the speckle pattern, resulting in an image with reduced random variations. Design and implementation of a compound imaging system is described, images of rubber tubes and porcine aorta are shown and effects on visualization are discussed. The speckle reduction is analyzed numerically and the results are found to be in excellent agreement with existing theory. An investigation of detectability of low-contrast lesions shows significant improvements compared to conventional imaging. Finally, possibilities for improving diagnosis of atherosclerotic diseases using MACI are discussed.

KEY WORDS: Atherosclerosis; compound imaging; detection; low contrast; spatial compounding; speckle reduction.

1. INTRODUCTION

The strength of the received electrical signal, due to the echo generated when an ultrasound pulse encounters a boundary in tissue, is very much dependent on the angle of incidence and the geometry of the boundary. Normally, the echoes generated at normal incidence are by far the strongest, as is well known by ultrasonographers and as has been shown theoretically.[1,2] An example is the strong received signal seen from the bottom and, to a less extent, from the top of a blood vessel, whereas the sides give rise to a much weaker received signal (an example is shown in figure 8).

One approach to reduction of the artifacts caused by the angle dependence is to scan a specific tissue region using several angles of insonification and then combine the information into a single image (denoted spatial compounding). By using multiple angles, a larger part of the boundaries in the tissue will experience near-normal incidence, thus giving strong received signals and well-defined boundaries. Another important effect of MACI is a reduction of the variance of the image speckle. As the image speckle is a statistical phenomenon[3,4] that changes for a given tissue region when the positions of the transmit and receive apertures are changed, images recorded using different beam angles will feature different speckle patterns. When information from multiple angles is combined, the speckle patterns of the individual images will be averaged, thus reducing the variance of the speckle (hereafter denoted 'reduced speckle') while maintaining a mean level that represents the mean reflectivity of

0161-7346/98 $18.00

the small point-like scatterers responsible for the speckle phenomenon. Approaches to speckle reduction using spatial compounding[5,6] and frequency compounding[7] have been considered in the literature. The reduced speckle may also contribute to a better definition of boundaries, as these are not disturbed by neighboring 'hills' and 'valleys' of the speckle pattern, which tend to make it difficult to distinguish between a truly uneven boundary and an even boundary with an uneven appearance due to the interference of the speckle. Finally, the reduced speckle might open possibility for better detection of low contrast regions or echo-strong microstructures (e.g., microcalcifications[8]) which can be difficult to distinguish as they are easily 'hidden' in the high-contrast speckle pattern.

A few spatial compound imaging systems have been constructed in the early 1980's[5,9,10] but since then the principle has primarily been considered theoretically.[8,11,12] The previously reported experimental results might in part have been limited by the state of transducer technology at that time (transducers with high frequency and low pitch not being available), limiting the possible angular ranges at higher frequencies.[9,10] Furthermore, the state of system technology at that time might have been an important limiting factor in total system performance. An example is the lack of possibility for creating correctly scan-converted images, as seen in the work of Shattuck and von Ramm.[5]

The system presented in this paper was designed specifically with the goal of improving B-mode images of atherosclerotic disease in the carotid arteries. As discussed previously, only part of the arterial wall is visualized well by conventional B-mode imaging. Thus, atherosclerotic disease is also likely to be insufficiently visualized. The degree of stenosis has been shown to be of importance,[13,14] but an increasing number of reports indicate that morphological features of the atherosclerotic plaque are important predictors of stroke.[15-18] Therefore, improvement of image quality might prove crucial, particularly considering that echo-poor lesions appear to be the most dangerous.[15,17] A better image quality might improve the prognostic information obtained, making it possible to optimize patient selection for prophylactic surgical removal of the plaque.

The MACI method can be implemented in most state-of-the-art, high-end ultrasound systems without major system redesign and additional cost, requiring a suitable transducer (low pitch and a fairly high number of transducer elements, e.g., ≥192) and phased array imaging possibility with a reasonable number of independent channels, e.g., ≥64. The only hardware changes required are in the control and scan conversion parts of the system.

Note that all comparisons in this paper are made between MACI and conventional B-mode imaging unless otherwise stated.

2. MULTI-ANGLE COMPOUND IMAGING SYSTEM

2.1 Principle of operation

The MACI system uses a conventional low-pitch linear array transducer. A subset of the elements is selected as the current active aperture and this aperture is used as a phased array to create a beam with one of the angles, θ_i, in the desired set of N_θ beam angles, θ_i, $i = 1,2,\mathrm{L}$, N_θ. The active aperture is then moved, as in conventional scanning, until scan lines originating from the entire extent of the linear array are recorded. Finally, the procedure is repeated for the next beam angle until data for all beam angles have been recorded. An illustration of the scan line locations is given in figure 1 for $N_\theta = 3$. A wideband transducer is used, which gives good range resolution and allows the use of different transducer excitation center frequencies without dramatic loss of emitted power and receive sensitivity. The excitation cen-

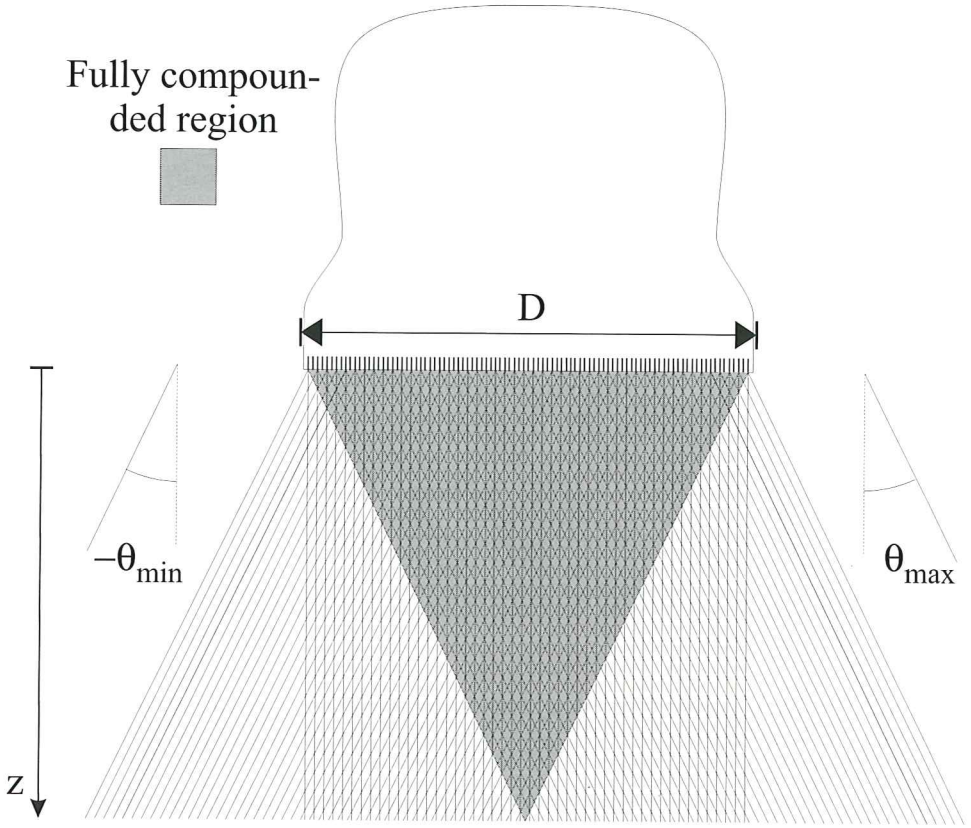

FIG. 1 Illustration of the scan line directions and origins used for creating a multi-angle compound image. The example shows an image consisting of sets of scan lines obtained using $N_\theta = 3$ different angles, $\theta_1 = -30°$, $\theta_2 = 0°$ and $\theta_3 = 30°$.

ter frequencies for beams with larger steering angles can thus be lowered in order to reduce the grating lobe energy to an acceptable level.

The extent of the fully-compounded image region is determined by the length of the array, D, and the most positive beam angle, θ_{max}, and most negative beam angle, θ_{min} (Fig. 1). The displayed image is not restricted to the fully-compounded region, as the full expanded sector region covered by the scan lines can be displayed, with the information outside the fully compounded region being based on the information from a reduced number of beam angles, this number being dependent on the actual location in the image. The width of the fully-compounded region, W_{reg}, is largest near the transducer and decreases linearly as the depth, z, from the transducer increases. The depth of zero compound region width, z_{max}, is easily found from the geometry in figure 1 to be:

$$z_{max}(D, \theta_{max}, \theta_{min}) = \frac{D}{\tan(\theta_{max}) - \tan(\theta_{min})} \tag{1}$$

An example of the maximum depth of the fully-compounded region for an array length of D = 40 mm and for numerically equal maximum and minimum beam angles, $\theta_{max} = -\theta_{min}$ is shown in figure 2.

The range of beam angles, $\theta_{max} - \theta_{min}$, determines the range of boundary orientation angles that will be insonified at normal or near-normal incidence. Further, the speckle reduction ef-

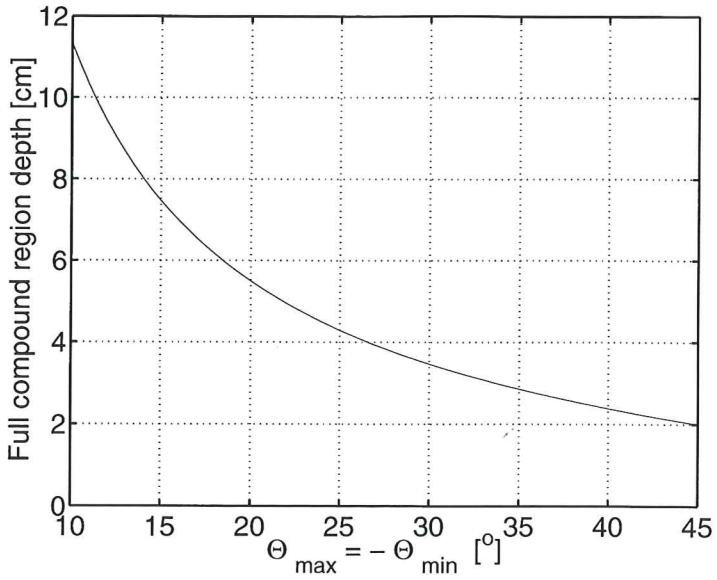

FIG. 2 Plot of the depth of the fully compounded region as a function of maximum beam angle for $D = 40$ mm and $\theta_{max} = -\theta_{min}$.

fect caused by the spatial and frequency compounding depends on the speckle patterns being markedly different from one scan line angle to another; this being the case only if the beam angles are sufficiently separated.

The postprocessing of the recorded scan lines to form the final image can be done in a number of ways. In this paper, the simplest possible approach is presented, namely to form an 'averaged' image, as averaging can be implemented in real time without a significant additional cost when compared to conventional B-mode scanners. An alternative to averaging is to use maximum amplitude detection, which leads to a good definition of boundaries, but a somewhat lowered speckle reduction.[3] Apart from the scan conversion, the recorded scan lines are processed conventionally.

2.2 System design considerations

The design choices that mainly determine the performance of a MACI system are the selection of reasonable transducer parameters for a given desired compound region geometry, i.e., number of elements, N_{elem}, center frequency, f_0, pitch (distance between centers of neighboring elements), p, kerf width (width of nonactive groove between elements), k, and element angular response. Limits might be imposed by the architecture of the transmit/receive system too, such as limits on the maximum number of scan lines in the image, delay resolution, etc. The transducer parameters must be chosen to allow compounding to the desired depth, while maintaining satisfactory acoustic performance at the extreme beam angles, that is, an acceptable low grating lobe level and an acoustic output sufficiently high to ensure an acceptable signal-to-noise ratio. Another limiting factor is the total array length, $D = N_{elem} p$, which must be chosen for a given clinical application to accommodate a good acoustical contact for the entire array when used for scanning the selected region of interest. As an example, for scanning the carotid artery region, a reasonable value would be $D = 40$ to 50 mm, whereas a value of $D = 80$ mm would be impractical, due to the anatomy of the human neck.

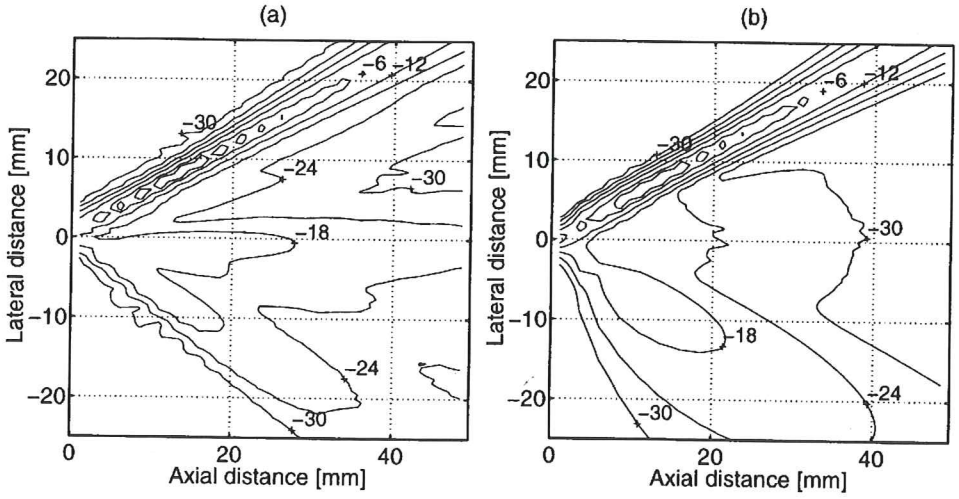

FIG. 3 Normalized contour plot of the pulse intensity integral of the transmitted field, using a beam angle of 30° and an excitation frequency of 5 MHz. (a) Data measured by hydrophone (0.5 mm diameter PVDF, type MH28-5, Force Institute, Brøndby, Denmark) and (b) data obtained using the field simulation program Field II. Contours are plotted at levels -3, -6, -12, -18, -24, and -30 dB. The hydrophone was tilted to point towards the center of the aperture at all measurement positions.

The selection of reasonable transducer parameters must often be done in an iterative way, as the influence of grating lobes on the contrast resolution of the image is not straightforward. However, by application of field simulation programs, e.g., Field II (http://www.it.dtu.dk/~jaj/field/field.html), based on the principles described in the work of Jensen and Svendsen,[19] it is possible to predict the level of the grating lobe quite accurately for a given beam angle, when transducer pitch, kerf width, electro-acoustic transfer functions, excitation waveform, transmit delay resolution, etc., have been determined or estimated.

For the experimental system presented here, the following parameters were chosen as a realistic compromise, partly dictated by the system limitations and the commercially-available transducers:

- Total array length: $D = 40$ mm.
- Number of elements: $N_{elem} = 192$.
- Pitch: $p = 208$ μm.
- Transducer center frequency: $f_0 = 7.5$ MHz.
- Transducer bandwidth (-6 dB): ≥ 70%.

The usable range of beam angles was estimated by a series of beam profile simulations to be approximately –25% to 25%. An example of measured and field simulated data for the emitted field for a beam angle of 30% and an excitation center frequency of 5 MHz is shown in figure 3.

The grating lobe level is predicted quite accurately using the field calculation program. Further, it can be concluded that a beam angle of 30% is not likely to give a good performance with the selected system, as the grating lobe is only 18 dB below the main lobe. Depending on the desired contrast resolution, it was found that the system performed satisfactorily with beam angles up to approximately 25% when the transmit excitation frequency was lowered from f_0 (7.5 MHz) to 5 MHz at larger angles (>15%), as this lowers the grating lobe level. The small deviations between the measured and the simulated fields are most likely due to nonideal vibrational behavior of the transducer elements; using a hydrophone, it

was demonstrated by field mappings that the angular responses of the individual elements were narrower than those predicted theoretically.

2.3 Distortion due to movement of tissue during scanning

A factor that may degrade MACI image quality is the increased recording time required when information from multiple angles is recorded. If conventional processing is used, the frame rate will approximately be reduced by a factor of N_θ, compared to conventional imaging. The smearing that will result from the movement of tissue will depend on the imaging geometry, the number of angles and the velocity of the tissue.

A worst case estimate of the movement distortion can be made once the recording procedure is defined. Assume that the desired axial depth of the image is z_{img}, the most negative and most positive beam angle, θ_{max}, are numerically equal, and that the number of scan lines for each individual angle is N_{scln}. If the trapezoidal expanded image format shown in figure 1 is used the required time for recording all scan lines at a single angle θ_i, $t_{\theta i}$, can be found to be:

$$t_{\theta i} = \frac{N_{scln} 2 z_{img}}{c_a \cos(\theta_i)}, \quad i = 1, \cdots, N_\theta \tag{2}$$

where c_a is the mean speed of sound assumed by the ultrasound system. Assume now that the information is recorded sequentially such that all information for the most negative angle is recorded first, then for the secondmost negative angle, etc., until at last, for the most positive angle. By careful inspection of the scan line origins and orientations in figure 1, it can be seen that when this recording procedure is used the maximum temporal separation, Δt_{max}, between scan lines from different angles through a specific tissue region can be approximated quite well by the time for recording $N_\theta - 1$ single-angle frames:

$$\Delta t_{max} = \sum_{i=1}^{N_\theta - 1} t_{\theta_i} \tag{3}$$

An estimate of the movement distortion when imaging the carotid artery can now be made. Assume a MACI image with $z_{img} = 40$ mm, $N_\theta = 6$ angles linearly spaced between –20° and 20°, $N_{scln} = 160$, and $c_a = 1{,}540$ m/s. The time for recording an entire compound image will then be 51 ms, corresponding to a compound image frame rate of 19 Hz. The maximum temporal separation between all the scan lines for a single spatial location will be $\Delta t_{max} = 43$ ms. The exact influence on the image quality can only be found if the exact tissue velocity pattern versus time is known for the area of interest, but here an estimate for the carotid artery will be given, based on movement data determined from scanning of carotid arteries at high frame rate. Published data[20] on the movement of a healthy carotid artery wall indicate a maximal dilation of approximately 0.75 mm, occuring over a time of approximately 0.25 s, while the dilation for a carotid artery with a small, clinically-insignificant plaque was found to be only 0.3 mm over 0.25 s. If the value of Δt_{max} is 43 ms and the above-mentioned data for the carotid arteries are used, the maximum displacement within a single compound image frame is found to be 0.13 mm for the healthy artery and 0.05 mm for the diseased artery. These shifts should be compared to a typical axial resolution of ~ 0.3 mm.

2.4 System implementation

2.4.1 System hardware

A block diagram of the system hardware is depicted in figure 4. A Pentium PC (133 MHz and 32 MB of RAM) is used as user interface, system controller and for processing of the received signals. The transmit part of the system is a parallel real-time transmit system with

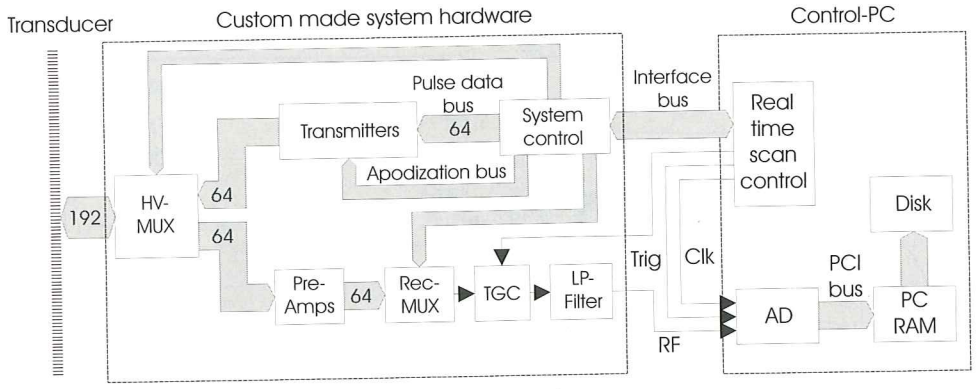

FIG. 4 Block diagram of the hardware of the experimental system used for multi-angle compound imaging.

fully programmable transmit delay (range 0 to 34 μs) and apodization control (range 0 to –25 dB). The delay resolution of the transmit system is 16.7 ns. The transmit system consists of: (a) a high voltage multiplexer (HV-MUX) that controls connection of the 192 transducer elements to the 64 transmit/receive channels of the system; (b) 64 transmitters; and (c) a system control board where transmit pulses are stored in RAM together with apodization information and aperture selection information. The receive system consists of: (a) 64 preamplifiers (Preamps); (b) a receive channel multiplexer (Rec-MUX) selecting one of the 64 channels for recording; (c) a time-gain control (TGC) amplifier; (d) an anti-aliasing lowpass filter (LP-Filter); and (e) a 12-bit analog-to-digital converter card (AD).

Clock signals, the voltages controlling the TGC and timing-related logic signals are generated by a real-time scan control (RTSC) board mounted in the PC, and interfaced via the PC ISA-bus. The AD-card is clocked externally by a clock from the RTSC to ensure that all sampling is synchronous to the transmit excitations, i.e., a very low time jitter is experienced between recorded single element radiofrequency (rf) signals, which is crucial when sampling the single element signals one at a time and beamforming off-line. AD-clocks of f_s = 20, 24, 30, 40 and 60 MHz can be selected, based on transducer center frequency and beamforming requirements.

Unfortunately, the experimental system is not capable of doing real-time imaging, due to the lack of a real-time digital beamformer, thus excluding *in vivo* investigations where movement distortion can be a problem. However, the system offers advantages as a research system, compared to most commercial systems, as access to received signals is possible at all stages in the signal processing chain (data can be saved on disk as single element rf data, rf scan lines, envelope scan lines, raw scan-converted image and log-processed and scaled image (TIFF-format)). The system has been designed to allow efficient recording and transfer of the single element data, using a PCI-bus based AD-card (CompuScope 6012/PCI, GaGe Applied Sciences, Montreal, Quebec, Canada). If data are recorded and transferred to the PC-memory (no beamforming while recording) a data acquisition rate for typical recording situations is 1,100 data segments of 3,500 samples per second, at a sampling rate of f_s = 30 MHz (corresponding to a 8 MB/s throughput), including the overhead between recordings for system setup (receive-MUX programming, HV-MUX programming, etc.). If the amount of recorded data is larger than the available PC memory, single element data must be beamformed to form rf scan lines or saved to disk and the acquisition rate is significantly lowered. A typical recording time for a conventional image (192 scan lines) is 2-3 minutes, when the beamforming is made during the recording and the beamformed rf scan lines are

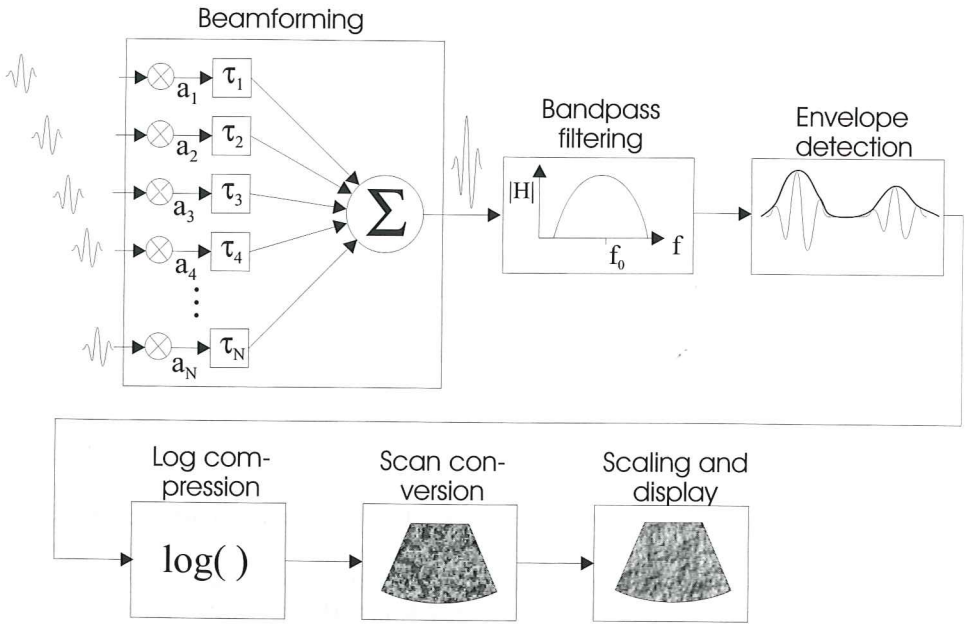

FIG. 5 Block diagram of the signal processing made in software in the experimental system used for recording data for multi-angle compound imaging.

saved to disk. The image can be displayed on the PC screen during recording, thus forming an entire ultrasound scanning system. Postprocessing and numerical analysis can subsequently be made off-line.

2.4.2 *Signal processing and software*

A schematic representation of the software-implemented signal processing of the received signals is shown in figure 5. The first part of the signal processing is made by a receive beamforming unit that weights (apodizes) and delays the individual single element rf signals and sums them into a rf scan line. For a given time (or equivalently depth), each single element signal number i is weighted by the weight a_i and delayed by the time τ_i, as illustrated in figure 5. The values of a_i and τ_i are updated with new values for every sample time $t=n/f_s$ of the single element input signal (i.e., fully-dynamic focusing and apodization). The apodization function also serves to increase the aperture size as the focal distance increases (by letting more elements having $a_i \neq 0$), thereby dynamically maintaining an extent of the active receive aperture corresponding to a receive F-number, F_{rec}, of 2 (F is the distance from the center of the aperture to the focal point divided by the aperture width). The transmit and receive apodization functions used for creating the data presented in this paper were all Hamming-weighting functions.[21]

The delay and apodization setup data to the beamforming unit are given as coarsely (and unevenly) sampled representations of the ideal delay and apodization functions for each element in order to reduce the amount of delay and apodization set-up data that need to be calculated and stored prior to the beamforming. The beamforming unit interpolates linearly between the input values to get the continuously-updated values. The delay system operates by dividing the desired delay at a given time into a coarse delay and a fine delay. The coarse delay is in units of the sampling time interval, $T_s = 1/f_s$, and can be implemented by simply shifting the signal an integer number of samples. When the coarse delay operation has been

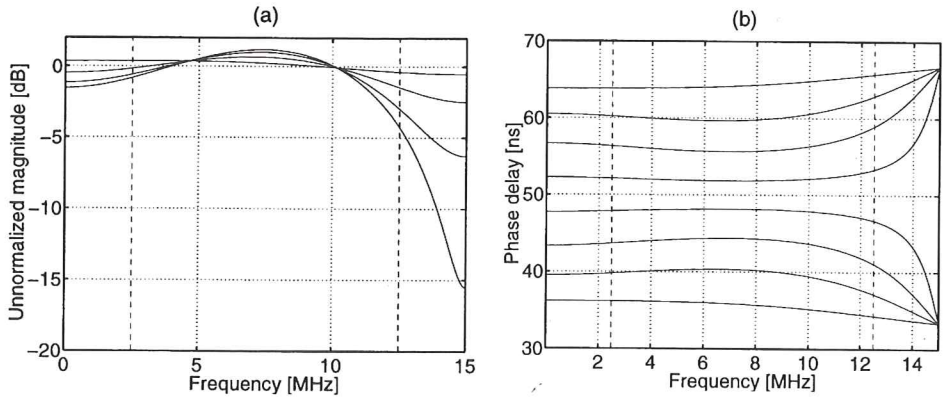

FIG. 6 (a) Magnitude and (b) phase delay for the filters of a filter bank containing 8 filters, implementing delays in increments of $T_s/8 = 4.2$ ns. The illustrated filter bank uses $f_s = 30$ MHz, $N_f = 8$ different filters and four coefficients per filter. The selected frequency band of interest was from 2.5 MHz to 12.5 MHz.

performed a small delay error of a fraction of T_s remains. The fine delay is implemented by filtering the shifted signal with a FIR fractional delay filter,[22] selected from a filter bank of N_f filters implementing equally-spaced delays of T_s/N_f. Thus, the resulting delay resolution is T_s/N_f. The filters were designed using a modified version of the algorithms described by Oetken et al.[23] An example of the amplitude and phase delay transfer functions of the fractional delay filters are shown in figure 6. Note that the amplitude variations in the frequency range of interest are less than 4.7 dB and that the phase delays are fairly well-behaved, exhibiting deviations from the desired delays of less than 2.7 ns.

Subsequent to beamforming, the rf scan lines are bandpass filtered for increasing the signal-to-noise ratio, then envelope detected using the Hilbert transform technique.[21] Finally, the scan lines are log compressed, scan converted, scaled and displayed. A weighting of the individual scan lines compensates for differences in amplitude resulting from the following factors: (a) changes in transmitted energy and receive sensitivity due to the angular response of the elements; (b) changes in transmitted energy due to different number of transmit elements used in the aperture; and (c) amplitude changes due to different transmit excitation frequencies. These compensations are crucial as the amplitude differences are dramatic, particularly due to the angular response of the elements. The scan conversion routine is made so that any pixel is an average over the number of scan lines at the region represented by the pixel, thus eliminating the drop in amplitude of the image that would result from a simple averaging, when the number of scan lines decreases outside the fully-compounded image region.

3. DATA ANALYSIS METHODS

3.1 Speckle statistics and reduction

The MACI method produces a speckle reduction effect in the compound images, i.e., the variance of the characteristic mottled appearance of the ultrasound image is reduced. The speckle is governed by random walk processes[24] determined by the scatterer locations, reflection phases, and reflection amplitudes within the resolution cell. The outcome of the processes varies with changes in: (a) the relative spatial positions of the transmit/receive

apertures and the scatterers; (b) the shape and size of the resolution cell; and (c) the frequency content of the interrogating pulse. Thus, the speckle patterns of the images recorded using different beam angles, and thus different aperture locations, exhibit speckle patterns that are uncorrelated or only partly correlated, leading to a reduction in the variance of the averaged compound image, as is well-known from statistics. For the case of completely uncorrelated images, the theoretically-predicted reduction in the variance will be $\sqrt{N_\theta}$, where N_θ is the number of uncorrelated images that are averaged.

An initial analysis of the speckle pattern can be performed using first-order statistics of the magnitude, V, of the received signals (found by the envelope-detection process). The expected value of V, $\mu_v = E\{V\}$, in units of its standard deviation, σ_v, is often referred to as the signal-to-noise ratio at a point, $\mathrm{SNR}_0 = \mu_v / \sigma_v$, and its inverse is denoted the speckle contrast.[3,4] The theoretical value of SNR_0 for a fully developed speckle pattern, in which the magnitudes of the received signals follow a Rayleigh distribution, is 1.91, whereas for an image compounded of N_θ uncorrelated images it is $1.91\sqrt{N_\theta}$.[3] If the images are partly correlated such that 'neighbor' angle images are partly correlated with a mean magnitude correlation coefficient of ρ, while images separated by more than one 'angle-step' are uncorrelated, the SNR_0 is given by:[12]

$$\mathrm{SNR}_0 = 1.91\sqrt{\frac{N_\theta}{1+2(N_\theta-1)\rho / \mathrm{N}_\theta}} \tag{4}$$

which is seen to yield the solution for uncorrelated images when ρ approaches zero. Observe that Shankar and Newhouse[12] use another correlation measure, therefore the correlation in their original equation appears squared. The relation between the two correlation measures is described in Goodman, Eq. (2.30).[25]

When compounding of images is made with the purpose of increasing SNR_0, it is important to investigate the correlation between the individual images, since the increase in SNR_0 will be smaller as the correlations between the images increase, as shown in Eq. (4). The conditions necessary for generating images with a sufficiently low correlation for achieving effective speckle reduction have been investigated in several publications. Typically, it has been investigated how large a fraction of the aperture width the active aperture should be translated between the individual recordings in order to obtain a certain degree of decorrelation[3,6,11,26] and a general agreement on a translation of about half the aperture width being optimal has been reached. These derivations[3,26] have been made using the following assumptions: (a) identical transmit and receive apertures are used; (b) cw theory (evaluated at the center frequency of the pulse) is used to describe the lateral variation of the beam; (c) the rotation of the point spread function is neglected, and consequently, the effects of scatterers leaving and entering the resolution cell are ignored; and (d) the lateral and axial descriptions of the range cells are separable. The solutions derived by Burckhardt[3] and Wagner[26] were valid only for apertures using rectangular amplitude windows and they are therefore not directly applicable for describing the experimental results presented here, as these were all created using Hamming amplitude-weighted apertures. An expression for the degree of decorrelation for Hamming-weighted apertures will therefore now be developed. In Wagner et al,[26] it is stated that that correlation between the intensity ($I = V^2$) at a given point in two single-angle images can be found from the lateral pulse-echo beam diffraction pattern, $p(x)$, for a given translation of the aperture, b:

$$\rho(b) = \left| \int |p(x)|^2 \exp(j2\pi 2bx / (z_0 \lambda_0)) dx \right|^2 \tag{5}$$

where λ_0 is the wavelength at the center frequency, z_0 is the axial distance to the observation point, and x is the lateral distance from the focal point. The integral in Eq. (5) is seen to corre-

spond to a spatial Fourier transform of the square of the lateral beam diffraction pattern, evaluated at a spatial frequency $f' = 2b/(z_0 \lambda_0)$. In Wagner et al [26] it is further stated that the correlation curve, $\rho(b)$, for the magnitude is very similar to the correlation curve for the intensity; therefore, it will be assumed that the correlation coefficients for the magnitude and the intensity are identical.

The expression for the lateral beam diffraction pattern near the focal point for a conventionally-focused Hamming-weighted aperture can be found from directivity pattern solutions in Ziomek, Chapt. 3.[27] Here, it is shown that if the aperture is focused using conventional quadratic focusing, then the beam diffraction pattern near the focal point can be described by the far-field beam diffraction pattern of the corresponding unfocused aperture. Therefore, it is straightforward to derive the beam diffraction pattern for the Hamming-weighted aperture. The amplitude variation, $a_h(x_a)$, over the Hamming-weighted aperture of length L is described by:

$$a_h(x_a) = [0.54 + 0.46\cos(2\pi x_a / L)]\,\mathrm{rect}(L) \tag{6}$$

where x_a is the lateral coordinate at the aperture and rect(L) is the rectangular amplitude window defined by:

$$\mathrm{rect}(L) = \begin{cases} 1, & |x_a| < L/2 \\ 0, & \text{otherwise} \end{cases} \tag{7}$$

The normalized directivity function for the Hamming-weighted aperture near the focal point, $D_h(x)$, can be found from the spatial Fourier transform of $a_h(x_a)$. The result can be found from Eqs. (3.3-14) and (3.3-52) in Ziomek[27] to be:

$$D_h(x) = \mathrm{sinc}\left(x/(F\lambda_0)\right) + \frac{0.46}{1.08}\left[\mathrm{sinc}\left(x/(F\lambda_0)+1\right) + \mathrm{sinc}\left(x/(F\lambda_0)-1\right)\right] \tag{8}$$

where $\mathrm{sinc}(x) = \sin(\pi x)/(\pi x)$ and F is the F-number ($F = z_0/L$). In the derivation, it is assumed that $z_0 >> x$, which is realistic for reasonably well-focused beams when the axial distance is not very small. The pulse-echo lateral beam diffraction pattern near the focal point, $p(x)$, can now be found as the product of the directivity for the transmit aperture, $D_{h,t}(x)$ and the directivity for the receive aperture $D_{h,r}(x)$:

$$p(x) = D_{h,t}(x)\, D_{h,r}(x) \tag{9}$$

The solution for the correlation as a function of aperture translation, $\rho(b)$, could be determined analytically by rather tedious derivations, but since $\rho(b)$ is very easily determined numerically using Eq. (5) this will not be attempted here. The experimentally-determined interimage correlations presented in subsection 4.2 are described as a function of angular separation, $\Delta\theta$, rather than as a function of aperture translation, b. However, it is straightforward to convert between the two representations by noting that $\Delta\theta = \tan(b/z_0)$. An example of a theoretically-determined correlation curve is presented together with experimentally determined data in figure 10.

3.2 Detectability of low contrast regions

A common problem in analysis of ultrasound images is to determine whether a lesion region with a low contrast compared to the background is present in the image or not. Unfortunately, the high contrast speckle pattern in the conventional image seems to obscure the decision making of the observer, thus increasing the uncertainty as to whether the region is a random variation in the background speckle pattern or an actual lesion. It is possible to de-

scribe this decision-making process numerically, based on the knowledge of the speckle statistics and on decision theory.

The numerical analysis of the detectability of low-contrast regions used in this paper follows the approach of previous papers.[28,4] The statistical analysis performed in reference 28 shows that the signal-to-noise ratio for detection of a lesion region for an optimal observer, SNR_{opt}, is determined by the relative difference in mean intensity between the lesion region and the background, and by the number of independent speckle correlation cells over the lesion area. The expression found for SNR_{opt}[28] is:

$$SNR_{opt} = \sqrt{M}\,\frac{I_1 - I_2}{\sqrt{I_1^2 + I_2^2}} \tag{10}$$

where M is the number of independent speckle correlation cells over the target area, and I_1 and I_2 are the mean intensities of the target area and the background, respectively. For a compounded image where N_θ uncorrelated images are compounded the expression for the detection signal-to-noise ratio, $SNR_{opt,\,comp}$ becomes:

$$SNR_{opt,comp} = \sqrt{MN_\theta}\,\frac{I_1 - I_2}{\sqrt{I_1^2 + I_2^2}} \tag{11}$$

since the number of independent speckle cells inside the target area is increased by a factor of N_θ. Note that the detection SNRs defined in Eqs. (10) and (11) can become positive and negative, depending on the intensity levels of the lesion area and the background area. Thus, it is the *numerical value* of the detection SNR that is of importance when trying to estimate whether a lesion region is detectable or not; the sign of the SNR simply describes whether the lesion region has positive or negative contrast relative to the background. Typical values estimated for the detection threshold for human observers are on the order of 2.[28] This value was found to be in good agreement with the subjective classifications of detectability made in this study, and will be used as a guideline for the detectability in the numerical analysis presented below.

In order to determine SNR_{opt} the speckle correlation cell sizes must be calculated or estimated. The cell sizes in the axial direction, S_{cz}, and lateral direction, S_{cx} are found from the following expressions:[4,25]

$$S_{cx} = \int_{-\infty}^{\infty} \frac{C_x(\Delta x)}{C_x(0)}\,d\Delta x, \quad S_{cz} = \int_{-\infty}^{\infty} \frac{C_z(\Delta z)}{C_z(0)}\,d\Delta z \tag{12}$$

where $C_x(\Delta x)$ and $C_z(\Delta z)$ are the spatial autocovariance functions of the intensity at displacements Δx and Δz in the x and z directions, respectively. Alternatively, S_{cx} and S_{cz} can be estimated from theoretical expressions,[4] based on system parameters, such as aperture sizes, focal distance, center frequency and transducer bandwidth. When the correlation cell sizes have been found, the number of speckle correlation cells, M, inside a circular lesion region of diameter d can be found by assuming an elliptical speckle cell size:

$$M = \frac{\pi d^2/4}{\pi S_{cx} S_{cy}/4} \tag{13}$$

4. RESULTS

All images presented in this section have been recorded using the following parameters, unless otherwise stated: Transmit excitation center frequencies of 7.5 MHz for beam angles ≤15° and 5 MHz for beam angles >15°. Transmit excitation pulse: 1.5 period pulse at the

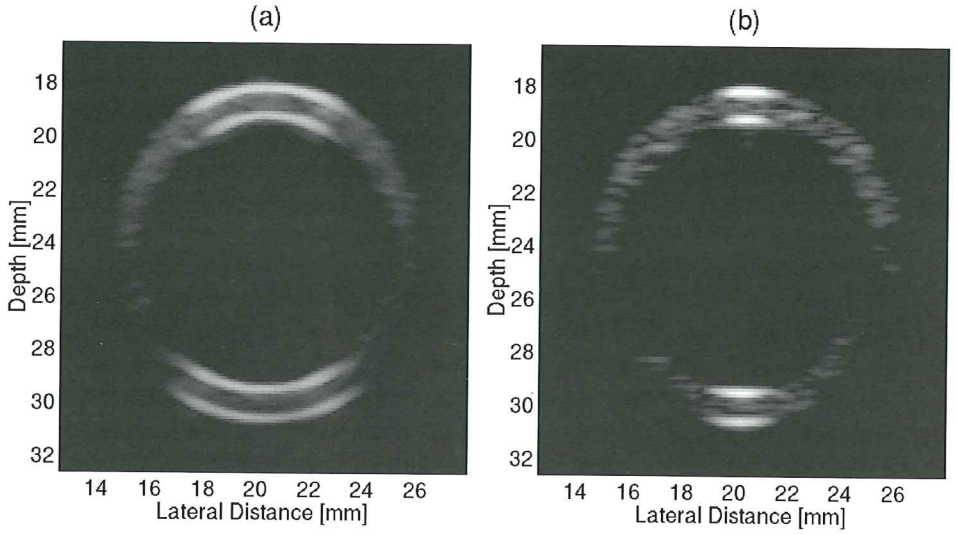

FIG. 7 (a) Compounded and (b) conventional images of a 12 mm outer diameter rubber tube in demineralized water. The depth of the fully compounded region is $z_{max} = 43$ mm.

center frequency. Transmit and receive apodization weightings: Hamming windows. Number of scan lines per angle: 192. Sampling frequency of received signals: 30 MHz. Transmit F-number: $F_{tx} = 4$, and receive F-number: $F_{rec} = 2$.

4.1 Visualization of boundaries

Figure 7 shows compound and conventional images of a rubber tube scanned in demineralized water. The regions extracted from the original images are 150x150 pixels (corresponding to app. 16x16 mm), centered at depth of 25 mm. $N_\theta = 6$ angles, spaced equally from -25° to 25° (angular step size, $\Delta\theta = 10°$), were used for creating the compound image. In this case, the real-time frame rates for MACI and conventional imaging would be 18 Hz and 114 Hz, respectively.

Notice that the boundaries, subjectively judged, seem to be better defined in the compounded image than in the conventional image. It is seen that the water/rubber boundary in figure 7a is well-defined in a region of the tube roughly corresponding to the angular range over which normal incidence is obtained. Outside this region, a less distinct improvement is seen, probably caused by the speckle-reduction effect. The visualization of the tube by conventional imaging depends to a large extent on the speckle pattern generated inside the wall of the tube. This is observed in figure 7b, where a well-defined visualization of the water/rubber boundary only exists in the immediate vicinity of the location where normal incidence is found. The visualization of the rubber tube outside this region is seen to mainly depend on the speckle pattern emerging from inside the wall of the rubber tube and not so much from the water/rubber boundary itself. If the speckle pattern inside the rubber wall had not been present, the difference between the images would probably have been even larger. Similar effects are likely to be present when investigating surfaces of varying roughness, with a smoother surface giving the largest improvement by compound imaging, since for a rough surface the scan lines used for the conventional imaging will also contain significant energy from boundaries at angles far from normal incidence.

In order to evaluate the effects of the MACI method on the visualization of blood vessels, a formalin-fixed thoracic porcine aorta (material described in Wilhjelm et al[29]) was scanned *in*

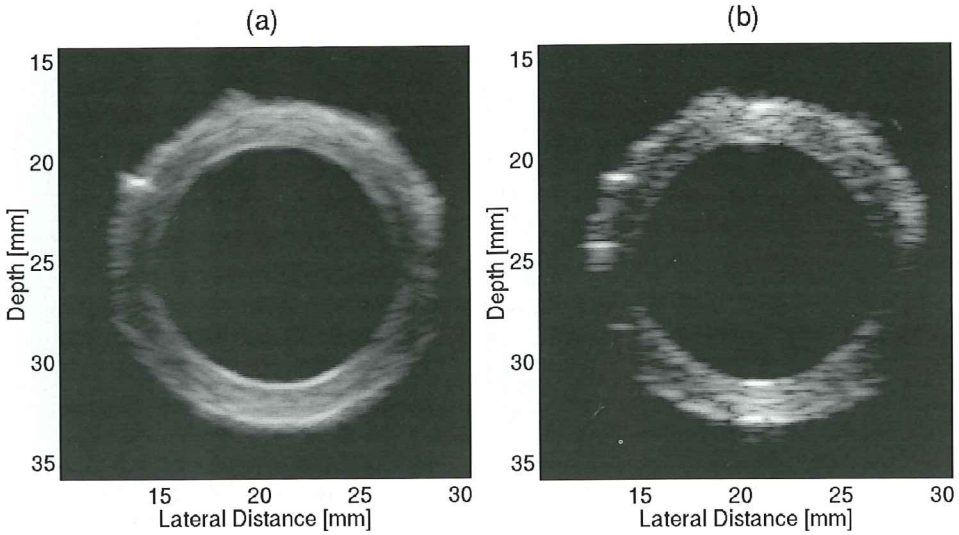

FIG. 8 Compounded (a) and conventional (b) images of a formalin-fixed thoracic porcine aorta scanned in demineralized water. The depth of the fully-compounded region is $z_{max} = 43$ mm.

vitro using MACI and conventional imaging. The resulting images are shown in figure 8, in which a 200x200 pixel region, located with its center at a depth of 25 mm, has been cut out of the image (the region size corresponds to 21x21 mm). $N_\theta = 6$ angles, spaced equally from -25° to 25° (angular step-size, $\Delta\theta = 10°$), were used for creating the compound image. The real-time frame rates for MACI and conventional imaging would be 16 Hz and 100 Hz, respectively. For the aorta shown in figure 8, the effects of MACI are similar to those seen when scanning the rubber tube shown in figure 7. A more consistent definition of the vessel wall is seen in the compounded image.

Finally, note a bright spot in the ten-o'clock direction in both the compound and conventional images in figure 8 and a bright spot in the nine-o'clock direction in the conventional image. The spot seen in the ten-o'clock direction is believed to be a variation in the acoustical properties of the sample, as it could be observed in all the individual subimages used for creating the compound image, as well as in the conventional image. The variation might either be due to a variation in the vessel wall itself or a tiny air bubble adhering to the vessel surface (the sample was degassed in vacuum before examination; however, a tiny bubble might have formed in the water of the scanning tank and adhered to the vessel). A visual inspection did not reveal any changes at the surface of the vessel capable of explaining the variation. Conversely, the spot seen in the nine-o'clock direction in the conventional image is neither present in the compound image nor in any of the individual images used for creating the compound image (which does not include an image at 0°), thus rendering it probable that the bright spot is a random variation in the speckle pattern inside the vessel wall being of high amplitude at a beam angle of 0°.

4.2 Speckle reduction

To quantitatively investigate the speckle reduction effect associated with MACI, a speckle generating phantom was scanned. The phantom is custom made (Danish Phantom Design, Jyllinge, Denmark) with a speed of sound c = 1,540 m/s and an attenuation of $\beta = 0.58$ dB/MHz/cm; it is comprised of a speckle-generating substance (coarse grain silicon carbide) mixed with an attenuation-generating substance (fine grain silicon carbide) and molded into

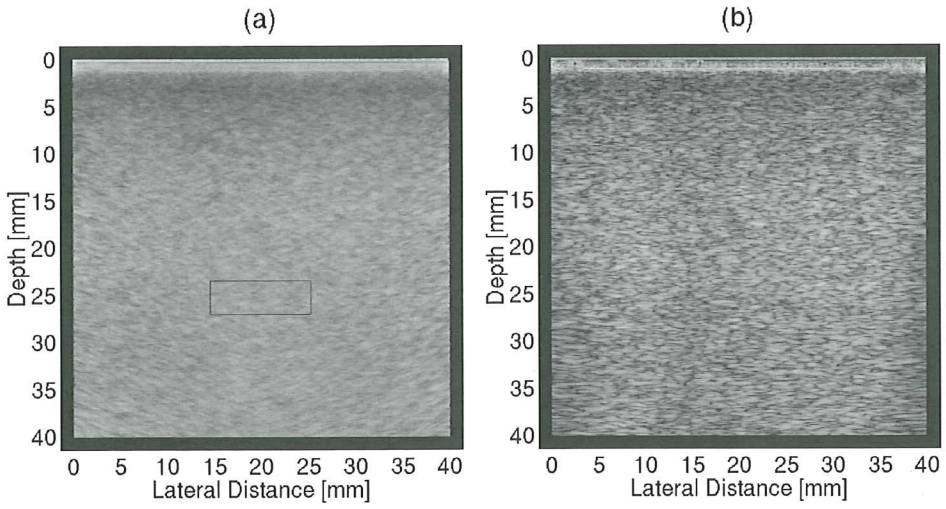

FIG. 9 (a) Compounded and (b) conventional speckle images. The outlined region, which is inside the fully compounded triangular region, is used for obtaining the numerical results. The depth of the fully-compounded region is $z_{max} = 43$ mm.

agar. The 40x40 mm region scanned in this experiment was designed to have a uniform scattering level. Images were recorded using an angular range of –25° to 25° in steps of $\Delta\theta = 5°$, i.e., $N_\theta = 11$ angles. Raw images (before logprocessing and scaling) were extracted for each of the 11 angles separately, for a compound image created using information from all 11 angles, and for a compound image comprised of information from $N_\theta = 6$ angles in –25° to 25° ($\Delta\theta = 10°$), respectively. The compound image made from all 11 angles is shown in figure 9a and the corresponding conventional image is shown in figure 9b.

Note that the contrast of the compound image is much lower than for the conventional image, which is a desirable property as the phantom does not contain any resolvable structures at the resolution of the system. First-order statistics and correlations between images were calculated for the region outlined in figure 9a. The location and size of the region was selected so that it was centered around the region of interest for the present system; the size is 150x50 pixels, corresponding to 10.7 x 3.6 mm. The resulting values of SNR_0 were calculated as described in subsection 3.1 and are shown in table 1. It is observed that the values in table 1 are all close to the theoretical value for SNR_0 for fully-developed speckle, which is 1.91.

The correlation between single-angle images was investigated for the selected region as a function of the angular separation, $\Delta\theta$, between the scan lines forming the images. The results of the correlation analysis are shown in figure 10, in which the theoretically predicted and experimentally-determined mean correlation coefficients, ρ, are shown as a function of angular separation. The theoretical curve was determined numerically using Eqs. (5), (8) and (9) with the parameters stated above and a wavelength corresponding to the 7.5 MHz transmit frequency. It is seen that images with an angular separation of only 5° are partly correlated, with a value of $\rho = 0.26$. The effect of this partial correlation is that the increase in

TABLE 1. SNR_0 as a function of beam angle for single-angle images.

Beam angle [°]	-25	-20	-15	-10	-5	0	5	10	15	20	25
SNR_0	2.00	1.99	1.92	2.04	2.02	1.98	1.94	1.90	1.90	2.04	2.15

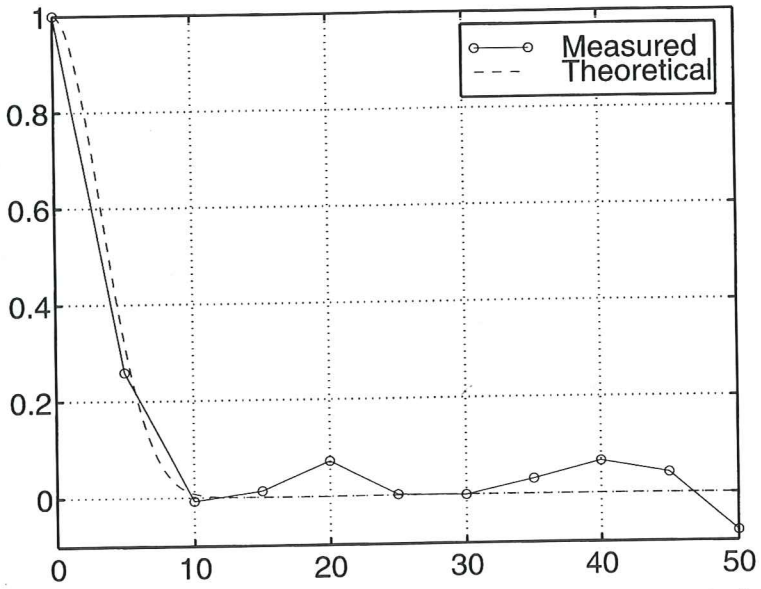

FIG. 10 The mean correlation between images recorded using different beam angles plotted as function of the angular separation between the scan lines forming the images. Note that 10 images are used for calculating ρ for 5° separation, 9 images for 10°, etc. The theoretically-predicted correlation curve is shown for comparison.

TABLE 2. SNR_0, improvement in SNR_0, and $N_{\theta,\,eff}$ for two compound images.

N_θ	Δθ	$SNR_{0,comp}$	$SNR_{0,comp}/SNR_{0,mean}$	$N_{\theta,eff}$
6	10°	4.77	2.40	5.76
11	5°	5.16	2.60	6.75

SNR_0 will be somewhat lower than the theoretically-predicted $\sqrt{N_\theta}$, if the images from all angles are compounded. In table 2, the SNR_0, $SNR_{0,comp}$, is shown for the two compounded images. Also shown are the improvements in SNR as compared to the conventional images and the corresponding effective number of independent images, $N_{\theta,\,eff}$, as estimated from the improvement in SNR_0:

$$N_{\theta,eff} = \left(\frac{SNR_{0,comp}}{SNR_{0,mean}} \right)^2 \tag{14}$$

where $SNR_{0,\,mean}$ is the mean value of the SNR_0 over all the single-angle images. The increase in SNR_0 observed when compounding the images from $N_\theta = 6$ angles with $\Delta\theta = 10°$, indicates that $N_{\theta,\,eff} = 5.76$ uncorrelated images are averaged, a result very close to the theoretical value of 6. This agrees well with the correlations shown in figure 10, which show that images separated by angles ≥ 10° are almost uncorrelated. The increase in SNR_0 observed when compounding the images from $N_\theta = 11$ angles with $\Delta\theta = 5°$, correspond to averaging only $N_{\theta,eff}$ =6.75 uncorrelated images. The large difference between $N_{\theta,\,eff}$ and N_θ is due to the partial correlation for beam angles with low separation. If the experimentally-determined correlation value ρ = 0.26 for images with 5° separation is used in Eq. (4), a value of $SNR_{0,comp}$ =

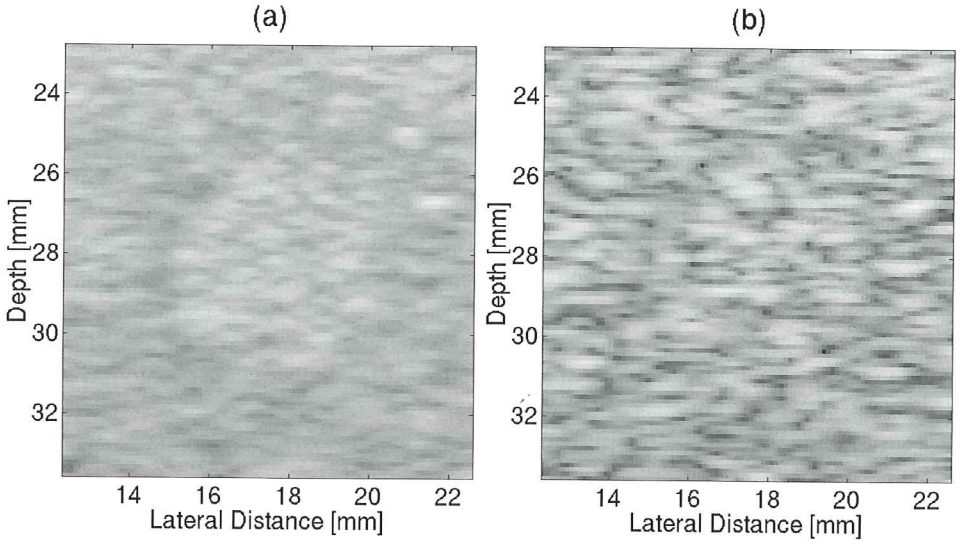

FIG. 11 (a) Compounded and (b) conventional images of a 5 mm diameter, +1.5 dB lesion in a low-contrast phantom. The depth of the fully compounded region is z_{max} = 75 mm.

5.98, corresponding to $N_{\theta,\,eff} = 7.47$, is found. Thus, the difference between the theoretical prediction of $N_{\theta,\,eff}$ and the experimentally-determined value is less than 10%.

4.3 Detection of low contrast regions

Detection of lesion regions with small contrast differences relative to the background was investigated experimentally using a low-contrast phantom (Model 111, Danish Phantom Design, Jyllinge, Denmark, http://www.fantom/suite.dk/). The phantom was scanned using MACI and conventional scanning and the visualization of the regions was examined visually and numerically. The phantom contains simulated circular lesion regions of 3, 5, and 10 mm diameter at increasing depth (approximately 15 mm, 30 mm and 50 mm); for each of the three region sizes, four regions exist, exhibiting differences in scattering level relative to the background of $\Delta\psi = -3, -1.5, 1.5$, and 3 dB ($\pm$ 1 dB), respectively. For this study, the regions of diameter 10 mm were located too deep, thus giving a total of 8 regions.

By experiment, it was found that, subjectively determined, a somewhat smaller angular range than that used above had the best performance for detection of low-contrast regions. Consequently, the compound scannings were made using $N_\theta = 5$ angles, spaced equally from $-15°$ to $15°$ (angular step size, $\Delta\theta = 7.5°$). Examples of regions extracted from compounded and conventional images of the 5 mm diameter, +1.5 dB lesion region in the phantom are shown in figure 11. The regions are 100x100 pixels, corresponding to 10.7 x 10.7 mm. The real-time frame rates for MACI and conventional imaging for this scanning situation would be 22 Hz and 114 Hz, respectively.

Subjectively determined, the circular lesion seems easier detectable in the compound image, compared to the conventional image in which the region is hardly visible. However, in the numerical analysis of the detectability of the region, it is estimated that the region would be detectable in both the compounded and conventional images, but in the conventional image, the SNR_{opt} for the region is quite close to the detection threshold.

In the following numerical analysis of the lesion detectability, the decision-making process is analyzed numerically, using the theory previously described in section 3.2. The correlation cell sizes for the system were found by evaluating Eq. (12) using autocovariance

functions in the x- and z-direction, respectively, estimated from regions of 150 x 300 pix extracted from the individual images forming the compound image in figure 9a. The m speckle correlation cell sizes over the angles used for generating the compound images of low-contrast phantom were found to be S_{cx} = 1 mm and S_{cz} = 0.5 mm.

When the theoretical expressions for S_{cx} and S_{cz} given in Wagner et al[4] are used (insert the appropriate values for the current set-up) the following values are found: S_{cx} = 1.1 mm = 0.3 mm.

The differences between the theoretically-predicted and the observed correlation cell si are mainly in the axial (range) direction. Possible reasons for the larger S_{cz} found in the perimental data are the use of a 1.5 period excitation pulse and a bandpass filter for reduc noise (Fig. 4), both of which result in a prolonged point spread function in the axial directi

The numerical analysis of the eight lesion regions in the low-contrast phantom was m by the following procedure:

1. The location of the circular lesion in the image was determined by moving a circl the appropriate diameter to a subjectively-determined best fit.
2. The average intensity of the lesion region, I_1, was calculated.
3. The average intensity of a background region, I_2, located as an annulus around the cular lesion region, was calculated.
4. The number of speckle correlation cells in the circular lesion region, M, was calcula by finding S_{cx} and S_{cz} as described above and then applying Eq. (13).
5. The optimal detection SNR for the conventional image, SNR_{opt}, and for the cc pounded image, $SNR_{opt,comp}$, were calculated using Eqs. (10) and (11), respectively.

The analysis procedure was carried out for the eight lesion regions (four scattering le and two diameters) and the results of the analysis are tabulated in table 3. It is seen that detection SNRs for the compounded images exceeded the detection threshold ($|SNR_{opt,comp}| \geq 2$) for all lesions except the +1.5 dB, 3 mm diameter region. The detect SNRs for the conventional images were above the detection threshold (i.e., $|SNR_{opt}| \geq$ only for the three easiest detectable positive contrast regions.

5. DISCUSSION

The effects of MACI on the visualization of a tubular structure have been investigated f rubber tube and for a porcine aorta scanned *in vitro*. It was found that the visualization of walls appeared to be improved due to a smoother border in the image over an increased an lar range as compared to the conventional image. The extent of the angular range in wh the visualization is improved is comparable to the angular range of the beams used for cr ing the image. However, compound imaging did not seem to give a significant improvem of the visualization of the vessel wall at the locations where no scan lines insonified the v at near-normal incidence, as seen in figure 8 at around the 4 o'clock and 8 o'clock directic

TABLE 3. SNR_{opt} for compounded and conventional images.

$\Delta\psi$ [dB]	-3	-3	-1.5	-1.5	1.5	1.5	3	3
d [mm]	3	5	3	5	3	5	3	5
SNR_{opt}	-0.7	-1.8	-1.1	-0.2	0.6	2.3	2.0	4.1
$SNR_{opt,\ comp}$	-3.6	-5.5	-2.8	-2.9	0.3	4.7	4.3	7.4

This observation is similar to the results presented in the work of Shattuck and von Ramm[5] and is probably due to the nature of the reflection phenomena contributing to the imaging of these parts of the vessel wall. The energy received from those locations on the vessel wall is caused by echoes from very small scattering structures or from surface roughness, i.e., nonspecular reflections. The echoes from such inhomogeneities are quite independent on angle of incidence and are thus imaged with similar strengths in the compounded and conventional images. The only difference is due to the speckle reduction effect seen in the compound images, which tends to make the outline of the wall somewhat more consistent. Thus, it appears that the improvement in visualization of boundaries is quite dependent on the characteristics of the reflecting surface, such as surface roughness, surface extent/geometry and on the internal reflecting structures inside the object, with smoother and larger surfaces giving the largest differences between the two imaging methods.

The analysis of the speckle statistics showed that the mean SNR_0 of the speckle patterns of the single-angle images was 1.99, which is very close to the theoretical value of 1.91 for Rayleigh-distributed speckle. These results are in better agreement with theory than previously-published results,[5] probably due to the access to unprocessed image data in our experimental set-up, whereas previously-published results were based on data retrieved after log compression and display. It was found that the angular separation required for obtaining uncorrelated speckle patterns is between 5° and 10°. The theoretical expression for the correlation that was developed shows a good agreement with the experimental results, with a theoretical correlation at $\Delta\theta = 5°$ of 0.32 while the experimentally-determined value was 0.26. The slightly-lower experimental value is most likely due to the fact that some of the effects leading to decorrelation (e.g., rotation of the resolution cell) are not included in the theoretical model. The effect of a partial correlation between images was clear when investigating the SNR_0 of compounded images; when compounding images with an angular separation large enough to ensure uncorrelated images, the improvement in SNR_0 was very close to the theoretical value of $\sqrt{N_\theta}$ for uncorrelated images, whereas compounding of partially correlated images showed a reduced effective number of uncorrelated images. The theoretical prediction for partly-correlated images was correct within 10% of the experimentally-determined value. In conclusion, the theoretical models for the speckle reduction were able to predict the speckle statistics and speckle reduction quite precisely.

When investigating detectability of low-contrast lesion regions with MACI, it was found beneficial to use a somewhat smaller angular range than that used for the best visualization of boundaries. The reason for the poorer performance when using a larger angular range might be the increased grating lobe level at larger beam angles, causing energy to be picked up by the grating lobes, thus obscuring the subtle differences in the scattering levels. Another possible reason is the poor sensitivity of the transducer elements at the larger beam angles which, in turn, leads to a significant amplitude scaling. This scaling may have elevated the electronic noise floor to a level that disturbed the detectability of the low-contrast regions significantly. It was found that application of MACI gave significantly-improved detection SNRs for all lesion regions but one. For the positive contrast regions, three regions were classified as detectable by both imaging methods; however, the conventional imaging was very close to the detection threshold in two cases, contrary to the compound imaging, which did exhibit detection SNRs above 4.0 in all three cases. For the four negative contrast regions investigated, none were classified as detectable by conventional imaging, whereas all were classified detectable by the compound images, i.e., a very clear improvement in detectability. In order to investigate whether the lack of detectability was due to the use of static images only, the negative contrast regions were also scanned using a commercial real-time ultrasound system (System 3535, with a 7.5 MHz linear array transducer (type 8541), B-K Medical A/S, Gentofte, Denmark). The subjectively-determined results ob-

tained during the real-time scanning showed that the same regions as in the conventional static images were classified as detectable.

Another area of application in which MACI might be beneficial is in the detection of very small echo-strong microstructures, such as breast microcalcifications that normally tend to be hidden in the speckle pattern.[8]

An important issue in ultrasound imaging is the influence of velocity inhomogeneities in the transmission medium located between the transducer and target area. The MACI method is more susceptible to degradation by uncertainties in speed of sound than conventional imaging. In the latter, a small defocusing and a translation of the image will result from errors in the assumed speed of sound, whereas for a compound imaging system, a blurring of the image will result due to the uncertainty of the range positions in the individual images being in different directions. The sensitivity of MACI to speed-of-sound variations also indicates that it will probably be of significant value to have the possibility for varying the mean speed of sound assumed by MACI systems, in order to minimize the image degradation. This could be done either by the operator or by some automated optimization routine. The MACI method might in this regard benefit by results from the intense research in methods for phase aberration correction.

A factor in MACI that might be of clinical importance is the reduction in frame rate. This may lead to smearing of the image if the tissue moves at a significant speed during scanning. Possible movement distortion was analyzed and it was found that for a typical recording situation at the carotid artery, the worst case tissue movement in a single compound image frame would be around one-third of the axial resolution cell size. Although these shifts are worst case estimates, these figures show that movement distortion is not negligible in a real-time implementation. The subjectively-determined smearing of the image may, however, be somewhat smaller, as the mean intraframe movement will be significantly smaller. Possible ways of reducing the movement distortion problem (by increasing the frame rate) could involve:

- Using multibeam processing, e.g., transmitting a single fairly-wide transmit beam and doing parallel receive processing of two (or more) scan lines. This can be extended all the way to full synthetic aperture recording, in which the recording time will be independent of the number of angles as the different scan lines are formed computationally after recording single element data.
- Restricting the compounding to a user-selected, limited region (as is usually done in CFM).
- Restricting the image region to the region corresponding to the conventional image.
- Lowering the number of beam angles.

An alternative to using MACI is to use coherent addition (synthetic aperture processing). Coherent addition will in theory improve both spatial and contrast resolution, as it is equivalent to using a single large aperture. However, coherent addition will neither produce speckle reduction effect nor lead to a less angle-dependent imaging of the tissue structures of interest, as only a single beam angle is used for creating the image. MACI and coherent addition also differ in their sensitivity to a spatially-varying speed of sound. In order for coherent addition to work well, the phase shifts of the received signal over the possibly quite large aperture, experienced due to varying speed of sound, must be smaller than maybe one-fifth of the period of the pulse. In MACI, signals are added after detection; therefore, acceptable phase shifts over the possible set of apertures may be of the order of half the length of the pulse. However, in MACI, other error sources exist as well, e.g., varying beam steering errors; therefore, a complete analysis and comparison of the possible error sources in the two techniques is quite complicated.

With respect to diagnosis of vascular disease, the obtained improvement in image quality might be important for future work. Although risk assessment to some degree is possible today, it is impossible to predict exactly who will suffer a stroke. Improved visualization of atherosclerotic plaque may prove crucial and the described results appear promising in this respect. Surface characteristics of the lesions have been shown to be of importance, but conventional B-mode imaging is inaccurate in predicting plaque surface irregularities (ulceration).[30,31] The present results indicate that compound imaging also may improve diagnosis of irregular/ulcerated plaque surfaces.

6. CONCLUSION

MACI has been shown to improve visualization of tissue boundaries as demonstrated by cross-sectional images of rubber tube phantoms and porcine aorta. Furthermore, a speckle reduction effect is seen; the experimentally-determined speckle statistics and speckle reduction have been analyzed and found to be in good agreement with the theoretically-expected values. The detectability of low-contrast regions in a phantom was found to be increased when compared to conventional B-mode imaging. For the low-contrast phantom investigated, seven out of eight regions were detectable using MACI whereas only three out of eight regions were detectable using conventional B-mode imaging. MACI therefore appears promising for improving the quality of ultrasound B-mode imaging.

ACKNOWLEDGEMENT

CADUS (Center for Arteriosclerosis Detection with UltraSound) is supported by the Danish Technical Research Council and the Danish Medical Research Council.

REFERENCES

1. Jespersen, S.K., Pedersen, P.C. and Wilhjelm, J.E.,The diffraction response interpolation method, IEEE Trans. Ultrason. Ferro. Freq. Contr. (submitted,1997).

2. Pedersen, P.C. and Orofino, D.P., Modeling of received ultrasound signals from finite planar targets, *IEEE Trans. Ultrason. Ferro. Freq. Contr. 3*, 303-311 (1996).

3. Burckhardt, C.B., Speckle in ultrasound B-mode scans, *IEEE Trans. Sonics Ultrason. 25*, 1-6 (1978).

4. Wagner, R.F., Smith, S.W., Sandrik, J.M. and Lopez, H., Statistics of speckle in ultrasound B-scan, *IEEE Trans. Sonics Ultrason. 30*, 156-163 (1983).

5. Shattuck, D.P. and von Ramm, O.T., Compounding scanning with a phased array, *Ultrasonic Imaging 4*, 93-107 (1982).

6. Trahey, G.E., Smith, S.W., and von Ramm, O.T., Speckle pattern correlation with lateral aperture translation: experimental results and implications for spatial compounding, *IEEE Trans. Ultrason. Ferro. Freq. Contr.* 33, 257-264 (1986).

7. Gatenby, J.C., Hoddinott, J.C., and Leeman, S., Phasing out speckle, *Phys. Med. Biol. 34*, 1683-1689 (1989).

8. Anderson, M.E., Soo, M.S., Bentley, R.C. and Trahey, G.E., The detection of breast microcalcifications with medical ultrasound, *J. Acoust. Soc. Amer. 101*, 29-39 (1997).

9. Berson, M., Roncin, A. and Pourcelot, L., Compounding scanning with an electronically steered beam, *Ultrasonic Imaging 3*, 303-308 (1983).

10. Carpenter, D.A., Dadd, M.J. and Kossoff, G., A multimode real time scanner, *Ultrasound Med. Biol. 6*, 285-289 (1980).

11. O'Donnell, M. and Silverstein, S.D., Optimum displacement for compound image generation in medical ul trasound, *IEEE Trans. Ultrason. Ferro. Freq. Contr.* 35, 470-476 (1988).

12. Shankar, P.M. and Newhouse, V.L., Speckle reduction with improved resolution in ultrasound images, *IEE Trans. Sonics Ultrason. 32*, 537-543 (1985).

13. European Carotid Surgery Trialists' Collaborative Group, MRC European carotid surgery trial: interim r sults for symptomatic patiens with severe (70-99%) or with mild (0-29%) carotid stenosis, *Lancet 337*, 1235-124 (1991).

14. North American Symptomatic Carotid Endarterectomy Trial Collaborators, Beneficial effect of carot endarterectomy in symptomatic patients with high-grade carotid stenosis, *New Engl. J. Med. 325*, 445-453 (1991).

15. Geroulakos, G., Domjan, J., Nicolaides, A., et al, Ultrasonic carotid artery plaque structure and the risk of c rebral infarction on computed tomography, *J. Vasc. Surg. 20*, 263-266 (1994).

16. Iannuzi, A., Wilcosky, T., Mercuri, M., Rubba, P., Bryan, F.A. and Bond, G. Ultrasonographic correlates carotid atherosclerosis in transient ischemic attack and stroke, *Stroke 26*, 614-619 (1995).

17. Langsfeld, M., Gray-Weale, A.C., and Lusby, R.J. The role of plaque morphology and diameter reduction the development of new symptoms in asymptomatic arteries, *J. Vasc. Surg. 9*, 548-557 (1989).

18. Sterpetti, A.V., Schultz, R.D., Feldhaus, R.D., et al, Ultrasonographic features of carotid plaque and the ri of subsequent neurologic deficits, *Surgery 104*, 652-660 (1988).

19. Jensen, J.A. and Svendsen, N.B., Calculation of pressure fields from arbitrarily shaped, apodized, and c cited ultrasound transducers, *IEEE Trans. Ultrason. Ferro. Freq. Contr. 39*, 262-267 (1992).

20. Bonnefous, O., Stenoses dynamics with ultrasonic wall motion images, in *Proc. IEEE Ultrasonics Sym* pp. 1709-1712 (1994).

21. Oppenheim, A.V. and Schafer, R.W., *Discrete-Time Signal Processing* (Prentice-Hall, Inc., 1989).

22. Laakso, T.I., V"alm"aki, V., Karjalainen, M. and Laine, U.K. Splitting the unit delay. *IEEE Signal Pr Mag.*, 30-60 (1996).

23. Oetken, G., Parks, T.W. and Schuessler, H.W., New results in the design of digital interpolators, *IEEE Tra Acoust., Speech Signal Proc. 23*, 301-309 (1975).

24. Goodman, J.W., Some fundamental properties of speckle, *J. Opt. Soc. Am. 66*, 1145-1150 (1976).

25. Goodman, J.W. , *Laser Speckle and Related Phenomena*, chapter: Statistical properties of laser speckle p terns, pp. 9-75 (Springer-Verlag, Berlin, 1975).

26. Wagner, R.F., Insana, M.F. and Smith, S.W., Fundamental correlation lengths of coherent speckle in med ultrasound images, *IEEE Trans. Ultrason. Ferro. Freq. Contr. 35*, 34-44 (1988).

27. Ziomek, L.J., *Underwater Acoustics* (Academic Press Inc., 1985).

28. Smith, S.W., Wagner, R.F., Sandrik, J.M. and Lopez, H., Low contrast detectability and contrast/detail a ysis in medical ultrasound, *IEEE Trans. Sonics Ultrason. 30*, 164-173 (1983).

29. Wilhjelm, J.E., Vogt, K., Jespersen, S.K. and Sillesen, H., Influence of tissue preservation methods on a rial geometry and echogenicity, *Ultrasound Med. Biol. 23*, 1071-1082 (1997).

30. Comerota, A.J., Katz, M.L., White, J.W.,and Grosh, J.D., The preoperative diagnosis of the ulcer atheroma, *J. Vasc. Surg. 11*, 505-510 (1990).

31. O'Leary, D.H., Holen, J., Ricotta, J.J., Roe, S. and Schenk, E.A., Carotid bifurcation disease: predictio ulceration with B-mode US, *Radiology 162*, 523-525 (1987).